

# Qubit interference at avoided crossings: The role of driving shape and bath coupling

Ralf Blattmann,<sup>1</sup> Peter Hänggi,<sup>1</sup> and Sigmund Kohler<sup>2</sup>

<sup>1</sup>*Institut für Physik, Universität Augsburg, Universitätsstraße 1, D-86153 Augsburg, Germany*

<sup>2</sup>*Instituto de Ciencia Materiales de Madrid, CSIC, Cantoblanco, E-28049 Madrid, Spain*

(Dated: March 8, 2022)

We derive the structure of the Landau-Zener-Stückelberg-Majorana (LZSM) interference pattern for a qubit that experiences quantum dissipation and is additionally subjected to time-periodic but otherwise general driving. A spin-boson Hamiltonian serves as model which we treat with a Bloch-Redfield master equation in Floquet basis. It predicts a peak structure that depends sensitively on the operator through which the qubit couples to the bath. The Fourier transforms of the LZSM patterns exhibit arc structures which reflect the shape of the driving. These features are captured by an effective time-independent Bloch equation which provides an analytical solution. Moreover, we determine the decay of these arcs as a function of dissipation strength and temperature.

PACS numbers: 03.67.-a, 03.65.Yz, 85.25.Cp, 73.21.La

## I. INTRODUCTION

The spectrum of a bistable quantum system as a function of the detuning typically forms avoided crossings. In particular in the regime between adiabatic following and non-adiabatic transitions, sweeping the detuning can induce a complex tunneling dynamics. Its archetype is a two-level system with a sweep linear in time for which the probability for non-adiabatic transitions is given by the famous Landau-Zener formula [1–4]. It predicts the splitting of the wavefunction into a superposition of the adiabatic qubit states, which means that the avoided crossing acts like a beam splitter. Replacing the linear switching by an ac field, results in a series of avoided crossings so that the wavefunction splits and recombines repeatedly—the quantum mechanical analogue of a Mach-Zehnder interferometer [5]. The resulting LZSM interference has been demonstrated in various experiments with solid-state qubits [6–12].

Going beyond the mere demonstration of interference, LZSM interferometry can be employed as a tool to determine the dephasing time of a charge qubit. The analysis of the interference pattern may be performed in “real space”, i.e. as a function of detuning and amplitude [11], or in Fourier space [13]. The latter type of analysis is based on the observation that the Fourier transform of LZSM patterns exhibit arc structures with a characteristic decay [14]. By comparing measured and computed patterns for a qubit, one can determine the inhomogeneous broadening as well as the faster decoherence induced by substrate phonons [13]. Since this procedure takes considerable numerical effort, any analytic knowledge may be helpful.

In this work, we reveal how the qubit-bath coupling operator and the shape of the driving influence the LZSM interference pattern. In Sec. II we describe the qubit as time-dependent spin-boson model [15] and introduce the Floquet-Bloch-Redfield formalism that provides our numerical solutions. Section III is devoted to the LZSM pattern in real space which is governed by the coupling operator to the bath. In Sec. IV we demonstrate that

its Fourier transform, by contrast, mainly depends the shape of the driving. Finally in Sec. V, we determine the decay of the arcs as a function of the bath parameters.

## II. MODEL AND MASTER EQUATION

### A. Qubit in a time-dependent field

We consider a qubit under the influence of a periodic driving described by the Hamiltonian

$$H(t) = \begin{pmatrix} \epsilon_0 & \Delta/2 \\ \Delta/2 & Af(t) \end{pmatrix}, \quad (1)$$

where  $\epsilon_0$  is a static detuning which is modulated by an ac driving with amplitude  $A$  and shape  $f(t) = f(t+T)$ . The gauge chosen in Eq. (1) is convenient for qualitative discussions, while the equivalent symmetrized Hamiltonian  $\tilde{H}(t) = \frac{1}{2}\{\epsilon_0 - Af(t)\}\sigma_z + \frac{\Delta}{2}\sigma_x$  is preferable for the numerical treatment.

While the most prominent example is the monochromatic  $f(t) = \cos(\Omega t)$ , our aim is to investigate LZSM interference for general periodic driving. In our numerical examples, we consider besides the purely harmonic driving with  $f_0(t) = \cos(\Omega t)$  also the shapes

$$f_1(t) = \cos(\Omega t) + 0.1 \cos(3\Omega t), \quad (2a)$$

$$f_2(t) = \cos(\Omega t) + \cos(2\Omega t), \quad (2b)$$

$$f_3(t) = \sin(\Omega t) + \sin(2\Omega t), \quad (2c)$$

where  $f_1$  and  $f_2$  are symmetric functions, i.e., they obey  $f(t_0+t) = f(t_0-t)$  for  $t_0 = 0$  and for  $t_0 = T/2$ . By contrast,  $f_3(t_0+t) = -f_3(t_0-t)$  is anti-symmetric. While  $f_1$  modifies the pure cosine driving only slightly, the other two shapes are qualitatively different because they possess several maxima and minima per driving period. As we discuss below in Sec. IV this has consequences for the structures observed in Fourier space, see Fig. 1[(g)–(i)].

## B. System-bath model

The influence of the environment on the system is modeled by a bath of harmonic oscillators given by the Hamiltonian  $H_{\text{env}} = H_b + H_{\text{int}}$  with  $H_b = \sum_{\nu} \hbar \omega_{\nu} a_{\nu}^{\dagger} a_{\nu}$ , and

$$H_{\text{int}} = \frac{1}{2} X \sum_{\nu} \hbar \lambda_{\nu} (a_{\nu}^{\dagger} + a_{\nu}), \quad (3)$$

where  $\omega_{\nu}$  are the frequencies of the oscillators, while  $\hbar \lambda_{\nu}$  are the system-oscillator coupling energies. For the qubit operator  $X$  that couples to the bath, we consider  $\sigma_x$  and  $\sigma_z$  as well as a linear combination of the two. According to their orientation on the Bloch sphere with respect to the driving, we refer to the coupling as transverse ( $\sigma_x$ ) and longitudinal ( $\sigma_z$ ), respectively. Moreover we assume that system and environment are initially uncorrelated, i.e., we choose an initial condition of the Feynman-Vernon type,  $\rho_{\text{tot}}(t_0) = \rho(t_0) \otimes R_{\text{env,eq}}$  for the total system density operator  $\rho_{\text{tot}}$ , with  $\rho(t_0)$  being the initial reduced density operator of the qubit, while  $R_{\text{env,eq}} \propto \exp(-\beta H_b)$  is the Gibbs state of the bath with inverse temperature  $\beta = 1/k_B T$ .

Starting from the Liouville-von Neumann equation  $i\hbar \dot{\rho}_{\text{tot}} = [H(t) + H_{\text{env}}, \rho_{\text{tot}}]$  for the total density matrix and applying standard techniques, one can derive the Markovian weak-coupling master equation [16]

$$\begin{aligned} \frac{d}{dt} \rho &= \mathcal{L}(t) \rho \quad (4) \\ &= -i[H(t), \rho] - \frac{1}{4} \int_0^{\infty} d\tau \left( \mathcal{S}(\tau) [X, [\tilde{X}(t-\tau, t), \rho]] \right. \\ &\quad \left. + \mathcal{A}(\tau) [X, \{\tilde{X}(t-\tau, t), \rho\}] \right), \end{aligned}$$

where  $\{A, B\} = AB + BA$  denotes the anti-commutator and  $\tilde{X}(t', t)$  is a shorthand notation for  $U^{\dagger}(t, t') X U(t, t')$ , with  $U$  being the propagator for the coherent qubit dynamics. The influence of the environment is subsumed in the symmetric and the antisymmetric bath correlation function,

$$\begin{aligned} \mathcal{S}(\tau) &= \frac{1}{2} \langle \{B(\tau), B(0)\} \rangle_{\text{eq}} \\ &= \frac{1}{\pi} \int_0^{\infty} d\omega J(\omega) \coth(\hbar\omega\beta/2) \cos(\omega\tau), \quad (5) \end{aligned}$$

$$\begin{aligned} \mathcal{A}(\tau) &= \frac{1}{2} \langle [B(\tau), B(0)] \rangle_{\text{eq}} \\ &= \frac{1}{\pi} \int_0^{\infty} d\omega J(\omega) \sin(\omega\tau), \quad (6) \end{aligned}$$

respectively, with the collective bath coordinate  $B(t) = \sum_{\nu} \lambda_{\nu} \{a_{\nu}^{\dagger} \exp(i\omega_{\nu} t) + a_{\nu} \exp(-i\omega_{\nu} t)\}$ . The angular brackets  $\langle \dots \rangle_{\text{eq}}$  denote the average with respect to the thermal equilibrium of the environment. In a continuum limit we consider the Ohmic spectral density  $J(\omega) = \pi \sum_{\nu} \lambda_{\nu}^2 \delta(\omega - \omega_{\nu}) \equiv 2\pi\alpha\omega e^{-\omega_c/\omega}$  with the high-frequency cutoff  $\omega_c$  eventually taken to infinity.

## C. Bloch-Redfield theory in Floquet basis

Since the system Hamiltonian is periodic in time we can apply the Floquet theorem which states that the corresponding Schrödinger equation possesses a fundamental set of solutions of the form  $|\Psi_{\alpha}(t)\rangle = e^{-i\varepsilon_{\alpha} t/\hbar} |\Phi_{\alpha}(t)\rangle$ , with the quasi-energies  $\varepsilon_{\alpha}$  and the Floquet states  $|\Phi_{\alpha}(t)\rangle = |\Phi_{\alpha}(t+T)\rangle$  [15]. They can be calculated from the eigenvalue equation  $\{H(t) - i\hbar\partial_t\} |\Phi_{\alpha}(t)\rangle = \varepsilon_{\alpha} |\Phi_{\alpha}(t)\rangle$ . Expressing the master equation Eq. (4) in the Floquet basis  $\{|\Phi_{\alpha}(t)\rangle\}$  [15, 16] yields

$$\frac{d}{dt} \rho_{\alpha\beta}(t) = \sum_{\alpha'\beta', k} e^{-ik\Omega t} \mathcal{L}_{\alpha\beta, \alpha'\beta'}^{(k)} \rho_{\alpha'\beta'}(t). \quad (7)$$

with the density matrix element  $\rho_{\alpha\beta} = \langle \Phi_{\alpha}(t) | \rho | \Phi_{\beta}(t) \rangle$  and

$$\begin{aligned} \mathcal{L}_{\alpha\beta, \alpha'\beta'}^{(k)} &= -i(\varepsilon_{\alpha'} - \varepsilon_{\beta'}) \delta_{\alpha, \alpha'} \delta_{\beta, \beta'} \delta_{0, k} \quad (8) \\ &+ \sum_{k'} (N_{\alpha\alpha', k'} + N_{\beta\beta', k'-k}) X_{\alpha\alpha', k'} X_{\beta\beta', k-k'} \\ &+ \delta_{\beta, \beta'} \sum_{k', \beta''} N_{\beta''\alpha', k-k'} X_{\alpha\beta'', k'} X_{\beta'\alpha', k-k'} \\ &+ \delta_{\alpha, \alpha'} \sum_{k', \alpha''} N_{\alpha''\beta', k'-k} X_{\beta'\alpha'', k-k'} X_{\alpha''\beta, k'}, \end{aligned}$$

the  $k$ th Fourier coefficients of the Liouville operator. We introduced the transition matrix elements

$$X_{\alpha\beta, k} = \frac{1}{T} \int_0^T dt e^{ik\Omega t} \langle \Phi_{\alpha}(t) | X | \Phi_{\beta}(t) \rangle \quad (9)$$

and  $N_{\alpha\beta, k} = N(\varepsilon_{\alpha} - \varepsilon_{\beta} + k\hbar\Omega)$  with  $N(\omega) = \alpha\omega n_{\text{th}}(\omega)$  and the bosonic thermal occupation number  $n_{\text{th}}(\omega) = (e^{\beta\hbar\omega} - 1)^{-1}$ .

In the long-time limit, the system relaxes to a steady state which obeys the time-periodicity of the driving,  $\rho_{\infty}(t) = \rho_{\infty}(t+T)$ . Hence we can use the Fourier decomposition  $\rho_{\infty}(t) = \sum_k e^{-ik\Omega t} \rho^{(k)}$  of the density operator to obtain

$$-i\hbar k\Omega \rho_{\alpha\beta}^{(k)} = \sum_{\alpha', \beta', k'} \mathcal{L}_{\alpha\beta, \alpha'\beta'}^{(k-k')} \rho_{\alpha'\beta'}^{(k')}. \quad (10)$$

This master equation avoids the common moderate [16] or full [17] rotating-wave approximation with respect to the driving frequency  $\Omega$  and, hence, is rather reliable [18]. In our case, numerical convergence is already obtained with  $|k| \leq 5$ , i.e., for truncation at the fifth sideband, even when the Floquet states may contain many more relevant sidebands. Thus the numerical effort for solving Eq. (10) stays at a tolerable level.

## D. Excitation probability

For the visualization of the LZSM interference pattern, one may in the absence of dissipation consider time-averaged transition probabilities from a particular initial

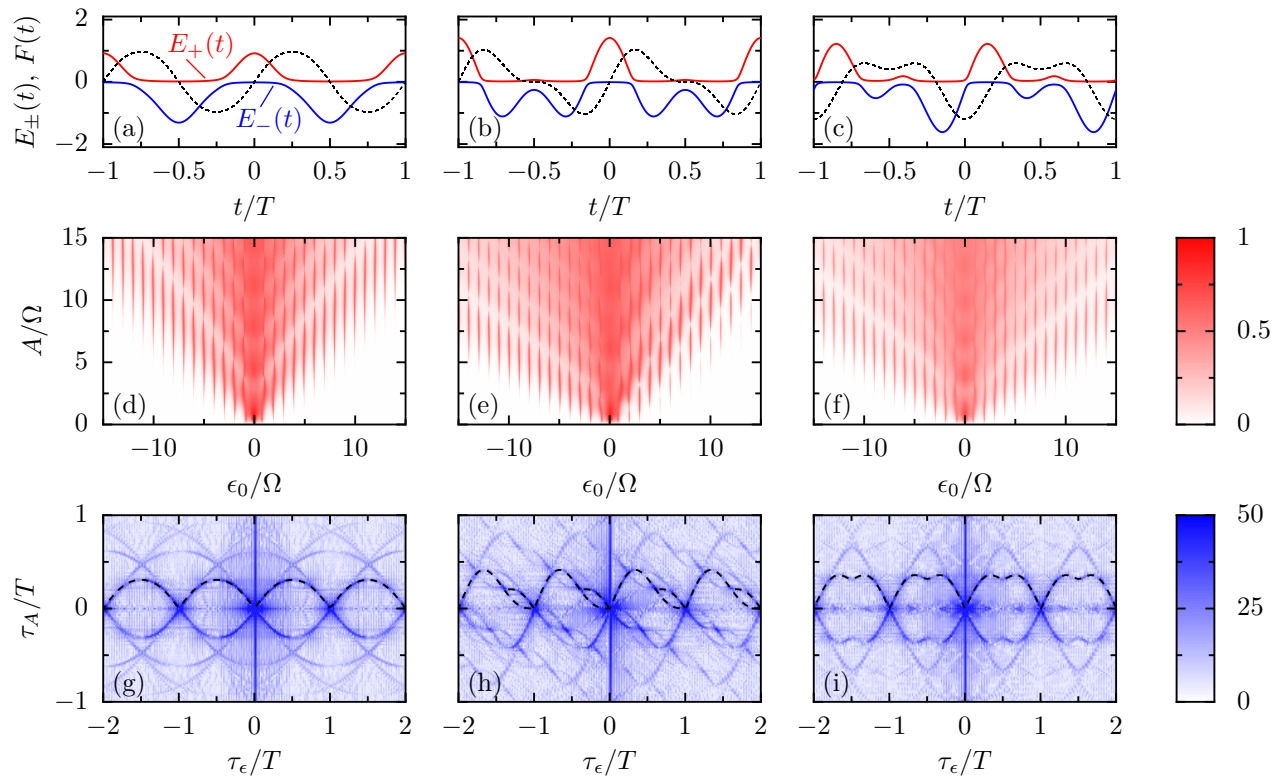


FIG. 1. (Color online) [(a)–(c)] Adiabatic energies  $E_{\pm}(t)$  (red and blue solid lines) of the Hamiltonian (1) in units of  $\hbar\Omega$  for vanishing static detuning,  $\epsilon_0 = 0$ , and the driving shapes  $f_1(t) - f_3(t)$  in Eq. (2). The dashed black line marks the integral of the driving,  $F(t)$ , in units of  $1/\Omega$ . [(d)–(f)] Resulting non-equilibrium populations in  $\epsilon_0$ - $A$  space. [(g)–(i)] 2D Fourier transform  $W(\tau_{\epsilon}, \tau_A)$  of the interference patterns, defined in Eq. (22). The dashed lines in the upper half plane mark the analytic expressions for the arc structure derived in Sec. IV. The patterns are computed with the stationary solution of the Bloch-Redfield master equation for the tunnel matrix element  $\Delta = 0.5\Omega$ , dissipation strength  $\alpha = 10^{-3}$ , temperature  $k_B T = 1/\beta = 0.1\hbar\Omega$ , and transverse qubit-bath coupling, i.e.,  $X = \sigma_x$  in Eq. (3).

state [5]. In the presence of a heat bath, however, the system state is in the long-time limit typically independent of the initial state. Therefore, we consider time averages of observables such as populations, e.g., of the diabatic state  $|\uparrow\rangle$ , or the excited state of the undriven qubit,  $|e\rangle$ . Since in the vast part of the parameter space considered, the qubit is strongly biased, i.e.,  $\Delta \ll |\epsilon_0|$ , the choice is of minor practical relevance. We here consider the latter namely the time-averaged probability for the qubit being in the excited state as a function of the static detuning  $\epsilon_0$  and the driving amplitude  $A$ ,

$$P_{\text{ex}}(\epsilon_0, A) = \frac{1}{T} \int_0^T dt \langle e | \rho_{\infty}(t) | e \rangle, \quad (11)$$

where  $\rho_{\infty}(t)$  is the periodic long-time solution of the master equation. Thus,  $P_{\text{ex}}$  directly relates to the Fourier coefficients in Floquet basis,  $\rho_{\alpha\beta}^{(k)}$ .

### III. INTERFERENCE PATTERN IN ENERGY SPACE

In order to give a first impression of our results, we depict in Figs. 1(d)–(f) the LZSM interference patterns for the driving shapes in Eq. (2) and transverse qubit-bath coupling. All three patterns exhibit resonance peaks whenever the detuning  $\epsilon_0$  matches with a multiple of the driving frequency. As a further condition for a significant non-equilibrium population, the amplitude must be so large that it reaches the avoided level crossing, which is the case for  $\min[f(t)] < \epsilon_0/A < \max[f(t)]$ . The peaks depend strongly on the amplitude and may even vanish. This represents a generalization of coherent destruction of tunneling found for sinusoidal driving [19], a phenomenon responsible for the characteristic vertical structure of LZSM patterns [5] which, in turn, can be explained within a Landau-Zener scenario [20]. Comparing panels (d)–(f), we can conclude that the patterns look qualitatively the same, despite the rather different driving shapes which are visible in the adiabatic energies of the qubit Hamiltonian (1) depicted in panels (a)–(c). The main differences stem from the fact that the harmonics

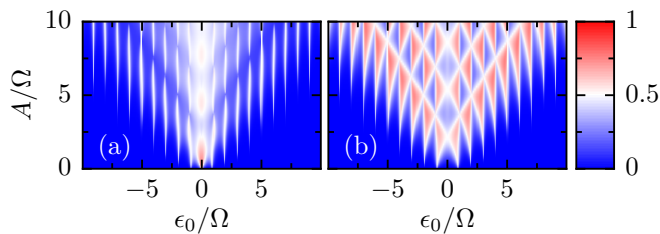


FIG. 2. (Color online) Non-equilibrium population  $P_{\text{ex}}$  as a function of the detuning  $\epsilon_0$  and the driving amplitude  $A$  for  $f(t) = \cos(\Omega t)$ . The qubit-bath coupling  $H_{\text{int}}$  is determined by  $X = \sigma_x$  (a) and  $X = \sigma_z$  (b), while  $\Delta = 0.5\Omega$ ,  $\alpha = 10^{-3}$  and  $1/\beta = 0.1\hbar\Omega$ .

with frequency  $2\Omega$  may change the maximum and the minimum value of  $f(t)$  and, thus, affect the above condition for significant excitations. For the driving shape  $f_2$ , this condition depends on the sign of  $\epsilon_0$ , which explains the asymmetry of the pattern in panel (e), which was also observed in Ref. [21].

### A. Influence of the qubit-bath coupling

In Fig. 2, we compare patterns for transverse and longitudinal qubit bath coupling, i.e., the coupling via  $\sigma_x$  and  $\sigma_z$ , respectively. Since we already noticed that the pattern in energy space is not very sensitive to the shape of the driving, we here restrict ourselves to the purely harmonic  $f_0(t) = \cos(\Omega t)$ . Let us first consider the transverse coupling. The resulting pattern [Fig. 2(a)] is characterized by resonance islands which as a function of the detuning  $\epsilon_0$  are Lorentzians. As a function of the amplitude  $A$ , their shape follows approximately the squares of Bessel functions. This behavior was predicted for the current through ac-gated double quantum dots [13, 22] and for the non-equilibrium population of a driven two-level system [5]. Moreover, it has been observed with good resolution in various experiments [6, 8, 10, 13, 14, 23].

If the bath couples longitudinally with respect to the driving, i.e., when both the ac field and the environment enter via  $\sigma_z$ , the pattern changes qualitatively. As can be appreciated in Fig. 2(b), the Lorentzian peaks turn into a triangular structure. This kind of bath coupling should be relevant for a charge qubit in a Cooper pair box driven by an ac gate voltage while being sensitive to environmental charge fluctuations. The LZSM pattern for such a case has been measured in Ref. [7] and indeed exhibits some similarity with Fig. 2(b). However, the resolution of the experimental data is not sufficient for an unambiguous comparison.

As a generalization of these two system-bath couplings, we also considered the coupling via the operator

$$X = \sigma_x \cos \theta + \sigma_z \sin \theta. \quad (12)$$

The mixing angle  $\theta$  varies from 0 to  $\pi/2$ , where the limits  $\theta = 0$  and  $\theta = \pi/2$  correspond to the transverse and the

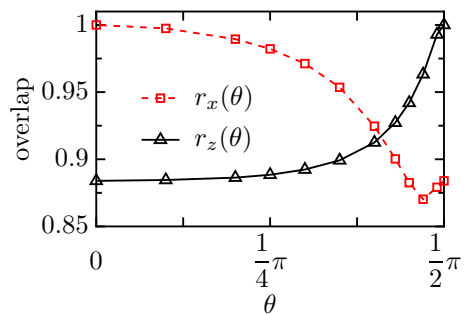


FIG. 3. Overlap of the interference pattern for the mixed coupling (12) with the patterns for the coupling operators  $\sigma_x$  (squares) and  $\sigma_z$  (triangles) as a function of the mixing angle. All other parameters are as in Fig. 2.

longitudinal case. This model captures, e.g., a superconducting charge qubit that interacts capacitively as well as inductively with the environmental circuitry. Then it is intriguing which dissipative influence dominates the LZSM interference. For this purpose, we define via the inner product of the patterns in parameter space the normalized overlaps  $r_{x,z}(\theta)$  of the  $\theta$ -dependent pattern with those for the bath couplings via  $\sigma_x$  and  $\sigma_z$ . Obviously, their limits are  $r_x(0) = 1 = r_z(\pi/2)$ .

The result shown in Fig. 3 reveals that upon increasing  $\theta$  from  $\theta = 0$ , i.e., augmenting the influence of  $\sigma_z$ , the pattern remains close to the one of Fig. 2(a). By contrast, the pattern for  $\sigma_z$  coupling is more sensitive to a small admixture of  $\sigma_x$ . Thus, unless the bath coupling via  $\sigma_z$  is much larger, we find the “usual” interference pattern of Fig. 2(a). This is consistent with the fact that in most experiments, one indeed finds such a LZSM pattern with Lorentzians [6, 8, 14, 23]. Notice however that this reasoning does not necessarily apply to LZSM patterns for the average current through open double quantum dots [10, 13], because there the dominating incoherent dynamics is the electron tunneling between the quantum dots and the leads. Moreover, the Hilbert space for a transport setup is larger since it must comprise states with different electron number.

Let us emphasize that the observed significant dependence of the long-time solution on the coupling is found even in the limit of very weak qubit-bath coupling and, hence, it is beyond a mere higher-order effect in the dissipation strength  $\alpha$ . This is in clear contrast to the stationary solution of the Bloch-Redfield equation for a time-independent problem, which generally is the grand canonical state, while possible deviations are of the order  $\alpha$  [24]. Nevertheless, we will be able to derive an effective time-independent Bloch equation for the driven qubit which captures the influence of the bath coupling operator quantitatively.

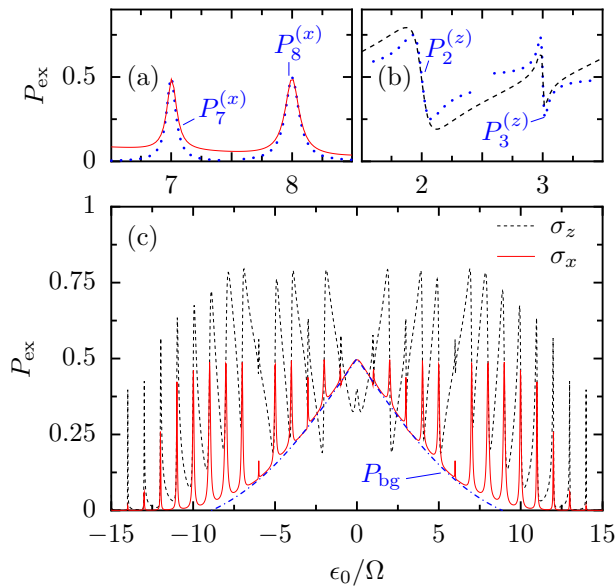


FIG. 4. (Color online) Non-equilibrium population  $P_{\text{ex}}$  shown in Fig. 2 as a function of the detuning  $\epsilon_0$  for the driving amplitude  $A = 10\Omega$ . (a) Comparison between numerical result with  $\sigma_x$  coupling obtained with the Bloch-Redfield master equation (solid red) and the analytical solution (19) for the resonances with  $n = 7, 8$  (dotted blue). (b) Comparison between numerical result with  $\sigma_z$  coupling (dashed black) and the analytical solution (21) for  $n=2,3$  (dotted blue). (c) Numerical results for  $\sigma_x$  and  $\sigma_z$  coupling plotted together with the analytical result for the off-resonant background predicted by Eq. (14).

## B. Analysis of the resonance peaks

While the two-dimensional interference patterns in Figs. 1(d)–(f) and 2 provide a comprehensive picture, the details of the resonance peaks are better visible in the horizontal slices shown in Fig. 4. They reveal that the peaks for transverse coupling indeed are Lorentzians. For longitudinal coupling, the peaks are anti-symmetric. Moreover, we witness a triangular shaped background with a roughly linear decays in  $|\epsilon_0|$  while being practically independent of the tunneling  $\Delta$ . Our aim is to explain these features within the Bloch equations for the qubit derived in Appendix A. We restrict the discussion to the limit of very low temperatures for which the interference pattern is most pronounced.

### 1. Off-resonant background

We start our considerations by noticing that at low temperatures, the dissipative dynamics is mainly a decay towards the qubit ground state. Since for small tunneling  $\Delta$  and large amplitude  $A$ , the (adiabatic) qubit levels form avoided crossings, the states  $|\downarrow\rangle$  and  $|\uparrow\rangle$  take turns in having lower energy, cf. the upper row of Fig. 1. Within an adiabatic description, we employ the Bloch equation (A4) and replace the  $\epsilon$ -dependent rates by their

instantaneous value to obtain for the  $z$ -component of the Bloch vector  $\vec{s} = \text{tr}(\vec{\sigma}\rho)$  the equation of motion

$$\dot{s}_z = -\Gamma[\epsilon(t)]s_z - \pi\alpha\epsilon(t), \quad (13)$$

where  $\epsilon(t) = \epsilon_0 + Af(t)$ . If the decay is sufficiently slow, we can replace the time-dependent coefficients by their time averages  $\bar{\Gamma} \equiv \overline{\Gamma[\epsilon(t)]} \approx \alpha(2A + \epsilon_0^2/A)$  and  $\overline{\epsilon(t)} = \epsilon_0$ . Then the steady-state solution  $s_z = \pi\alpha\epsilon_0/\bar{\Gamma}$  corresponds to the non-equilibrium population

$$P_{\text{bg}} = \frac{1}{2} - \frac{\pi\epsilon_0 A}{4A^2 + 2\epsilon_0^2}. \quad (14)$$

The dashed-dotted line in Fig. 4 (c) shows that this estimate indeed describes the triangular shaped background rather well which, in turn, confirms the underlying adiabatic picture.

### 2. Lorentzian peaks for the transverse coupling via $\sigma_x$

An analytic expression for the resonance peaks can be found within an approximation scheme for close-to-resonant excitation [5, 22]. For a bath coupling via  $\sigma_x$ , the calculation is practically the one given in the appendix of Ref. [5]. We sketch it briefly so that we can later highlight the differences to the case of a bath coupling via  $\sigma_z$ .

Embarking with the master equation (4) we consider the limit  $\epsilon_0 \gg \Delta$  and assume that the driving frequency is close to resonance, i.e.,  $n\Omega = (\epsilon_0^2 + \Delta^2)^{1/2} \approx \epsilon_0$ . In this regime the tunneling contribution, proportional to  $\Delta$  represents a perturbation to the free dynamics governed by  $\frac{1}{2}\{\epsilon_0 + f(t)\}\sigma_z$ . In order to capture the coherent dynamics in large part, we apply the unitary transformation  $U(t) = \exp\{-i\phi(t)\sigma_z/2\}$  with the time-dependent phase  $\phi(t) = n\Omega t + AF(t)$ , where

$$F(t) = \int_0^t dt' f(t') \quad (15)$$

obeys the  $T$ -periodicity of the driving since  $f(t)$  by definition vanishes on average. Then we obtain the interaction picture Hamiltonian  $U^\dagger(t)H(t)U(t) - i\hbar U^\dagger(t)\dot{U}(t)$ . Averaging over the driving period  $T$  results in the effective Hamiltonian

$$H_{\text{eff}} = -\frac{\delta_n}{2}\sigma_z + \frac{\Delta_n}{2}\sigma_x, \quad (16)$$

with the detuning  $\delta_n = n\hbar\Omega - \epsilon_0$  and the effective tunnel matrix element

$$\Delta_n(A) = \frac{\Delta}{T} \int_0^T dt e^{in\Omega t - iAF(t)}. \quad (17)$$

The latter obviously is the  $n$ th Fourier coefficient of  $\Delta \exp\{-iAF(t)\}$ , a property that will prove useful. This generalizes the result for purely harmonic driving,  $\Delta_n =$

$\Delta J_n(A/\Omega)$  with the  $n$ th order Bessel function of the first kind, to arbitrary but periodic shapes  $f(t)$ . The corresponding equation of motion for the Bloch vector reads  $\dot{\vec{s}} = \vec{B}_{\text{eff}} \times \vec{s}$ , where  $\vec{B}_{\text{eff}} = (\Delta_n, 0, -\delta_n)^T$ .

For the dissipative dynamics, we distinguish two limiting cases. First, during the stage at which the qubit passes through the crossing, the tunneling term  $\Delta\sigma_x/2$  dominates in the Hamiltonian (1), while the qubit-bath coupling essentially commutes with the Hamiltonian. Thus, it induces pure dephasing but no decay. Since for an Ohmic bath, the dephasing rate (A7) is proportional to the temperature, it can be neglected in the limit under consideration.

For most of the time, however, the qubit Hamiltonian is dominated by the term proportional to  $\sigma_z$  so that the bath causes transitions between the eigenstates  $H_{\text{eff}}$ . We describe them by the Bloch equation (A4) which together with the effective coherent dynamics reads

$$\dot{\vec{s}} = \begin{pmatrix} -\Gamma/2 & -\delta_n & 0 \\ \delta_n & -\Gamma/2 & \Delta_n \\ 0 & -\Delta_n & -\Gamma \end{pmatrix} \vec{s} - \begin{pmatrix} 0 \\ 0 \\ \Gamma \end{pmatrix}. \quad (18)$$

Notice that since we are only interested in the stationary state, we can ignore possible driving-induced renormalizations of the decay rates [25] and treat  $\Gamma$  as phenomenological parameter. However, we like to stress that our numerical treatment captures this renormalization. The steady state  $\vec{s}(\infty)$  is easily obtained by matrix inversion and provides the non-equilibrium population

$$P_n^{(x)} = \frac{1}{2} \frac{\Delta_n^2/2}{(\epsilon_0 - n\Omega)^2 + \Delta_n^2/2 + \Gamma^2/4}. \quad (19)$$

While this expression holds close to the  $n$ th resonance, it vanishes far-off. Therefore, the global picture is simply given by the sum of the contributions of all resonances and reads  $P_{\text{ex}}^{(x)} = \sum_n P_n^{(x)}$ . Such expressions have been found not only for non-equilibrium populations of driven qubits [5, 14] but also for the dc current through double quantum dots [13, 22].

In Fig. 4(a), we compare the numerically computed interference pattern for the  $\sigma_x$  coupling with the analytical solution (19) at various resonances. While close to the resonances, i.e. for  $\delta_n \ll \Delta$ , the agreement is almost perfect, we observe small deviations between the resonances which mainly stem from the off-resonant background discussed above.

### 3. Anti-symmetric resonances for the longitudinal coupling via $\sigma_z$

For longitudinal coupling, the situation is complementary to the transverse case. Outside the crossing, the bath couples to a good quantum number of the qubit and, thus, creates pure dephasing negligible at low temperatures. Thus, dissipative transitions are only induced close to the crossing. Therefore we obtain the corresponding

Bloch equations by cyclic permutation of the dissipative terms in Eq. (18) which yields

$$\dot{\vec{s}} = \begin{pmatrix} -\Gamma & -\delta_n & 0 \\ \delta_n & -\Gamma/2 & \Delta_n \\ 0 & -\Delta_n & -\Gamma/2 \end{pmatrix} \vec{s} - \begin{pmatrix} \Gamma \\ 0 \\ 0 \end{pmatrix}. \quad (20)$$

Its stationary solution provides the non-equilibrium population

$$P_n^{(z)} = \frac{1}{2} + \frac{(\epsilon_0 - n\Omega)\Delta_n}{(\epsilon_0 - n\Omega)^2 + 2\Delta_n^2 + \Gamma^2/2}. \quad (21)$$

Since now the qubit decay occurs only during the short stages when the levels cross, the phenomenological rate  $\Gamma$  is expected to be considerably smaller than for  $\sigma_x$  coupling.

In Fig. 4(b), we compare the numerically computed interference pattern obtained with  $\sigma_z$  coupling with the analytical solution (21) for  $n = 2, 3$ . Again, close to a resonance the analytics and the numerical solution agree rather well. Far from resonance, however, expression (21) decays only slowly and, the global picture is beyond the simple summation of all  $P_n^{(z)}$ . Exactly on resonance, i.e., for  $\epsilon_0 = n\Omega$ , the second term of Eq. (21) vanishes and, hence, the excitation probability becomes  $P_{\text{ex}}^{(z)} = 1/2$  for all  $n$ . This fact together with the asymmetry of the structure implies that close to each resonance, we find a region with  $P_{\text{ex}}^{(z)} > 1/2$ . Such population inversion has been found also for driven qubits with other structureless bath spectral densities [26].

## IV. INTERFERENCE PATTERN IN FOURIER SPACE

While we found that the interference patterns in real space depend only weakly in the shape of the driving, the opposite is true for their 2D Fourier transform shown in Figs. 1(g)–(i). For the symmetric driving functions  $f_1$  and  $f_2$ , we find a pronounced arc structure at  $\tau_A = 2F(\tau_\epsilon/2)$  and  $\tau_A = 2F(\tau_\epsilon/2 + T/2)$ , cf. the dashed black lines in panels (a) and (b). They can be explained within the stationary-phase treatment of the LZSM interference scenario [14]. However, there emerge several features that are beyond. Most significantly in panel (i), we find that for the anti-symmetric driving with  $f_3$ , the structure is different from the corresponding  $F(\tau_\epsilon/2)$  depicted by the dashed line in panel (c). Moreover, the driving  $f_2$  yields additional arcs close to the origin. There also emerge higher-order replica of the arcs which have been found both experimentally [13, 14] and theoretically [13].

For an analytical approach to the arc structure, we consider  $P_{\text{ex}}(\epsilon_0, A) = \sum_n P_n^{(x)}(\epsilon_0, A)$  derived Sec. III B 2 and define its Fourier transform as

$$W(\tau_\epsilon, \tau_A) = \int \frac{d\epsilon_0}{2\pi} \frac{dA}{2\pi} e^{-i\epsilon_0\tau_\epsilon} e^{-iA\tau_A} P_{\text{ex}}(\epsilon_0, A). \quad (22)$$



The  $\epsilon_0$ -integral can be evaluated readily to yield

$$W(\tau_\epsilon, \tau_A) = \frac{1}{4\pi} \int dA e^{-iA\tau_A} \sum_n \frac{\Delta_n^2}{\Gamma_n^*} e^{-in\Omega\tau_\epsilon} e^{-\Gamma_n^*|\tau_\epsilon|}, \quad (23)$$

with the resonance width  $\Gamma_n^* = (\Delta_n^2/2 + \Gamma^2/4)^{1/2}$ .

### A. Overdamped limit

The remaining  $A$  integral in (23) can be evaluated directly in the over-damped limit  $\Gamma \gg \Delta$  in which  $\Gamma_n^* \approx \Gamma/2$  and, thus,

$$W(\tau_\epsilon, \tau_A) = \frac{1}{2\pi\Gamma} \int dA e^{-iA\tau_A} \sum_n \Delta_n^2 e^{-in\Omega\tau_\epsilon}. \quad (24)$$

Focusing on the range of small  $\tau_\epsilon$ , we have neglected the last exponential in Eq. (23). To proceed, we evaluate the sum

$$\sum_n \Delta_n \cdot \Delta_n e^{-in\Omega\tau_\epsilon}, \quad (25)$$

where the two factors are easily identified as the  $n$ th Fourier coefficients of  $\exp\{-iAF(t)\}$  and  $\exp\{-iAF(t + \tau_\epsilon)\}$ , respectively, cf. the definition of  $\Delta_n$  in Eq. (17). Thus, expression (25) represents the inner product of these exponentials. According to Parseval's theorem, it can be written in the time domain to read

$$\frac{1}{T} \int_0^T dt e^{iAF(t)} e^{-iAF(t+\tau_\epsilon)}. \quad (26)$$

We symmetrize the integrand via the substitution  $t \rightarrow t - \tau_\epsilon/2$  and perform the  $A$ -integration to obtain

$$W(\tau_\epsilon, \tau_A) = \frac{1}{T} \int_0^T dt \delta(\tau_A - G(t, \tau_\epsilon)) \quad (27)$$

$$= \frac{1}{T} \sum_{t_i} \frac{1}{|g(t_i, \tau_\epsilon)|}, \quad (28)$$

where

$$G(t, \tau_\epsilon) = F(t + \tau_\epsilon/2) - F(t - \tau_\epsilon/2), \quad (29)$$

$$g(t, \tau_\epsilon) = f(t + \tau_\epsilon/2) - f(t - \tau_\epsilon/2). \quad (30)$$

The sum in Eq. (28) has to be taken over all times  $t_i$  that fulfill  $\tau_A = G(t_i, \tau_\epsilon)$ .

Expressions (27) and (28) allow us to extract the arc structure by the following reasoning. On the one hand, the argument of the delta-function in Eq. (27) specifies the times  $t_i$  that contribute to the integral. On the other hand, the most significant contributions to  $W$  stem from regions where the denominator in Eq. (28) vanishes. Thus, the structure is determined by the conditions

$$0 = g(t, \tau_\epsilon), \quad (31)$$

$$\tau_A = G(t, \tau_\epsilon), \quad (32)$$

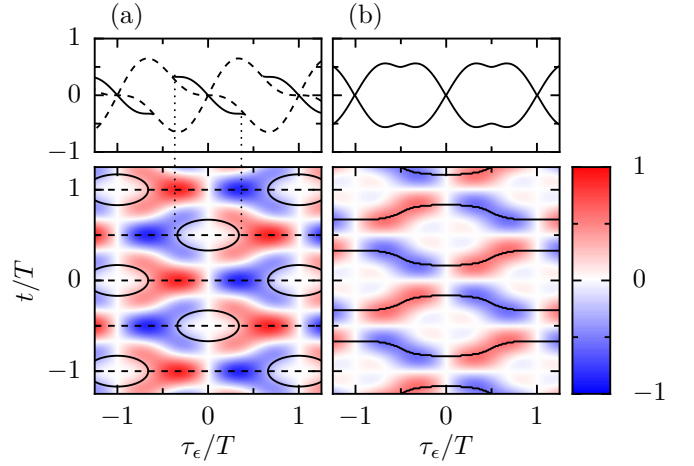


FIG. 5. (Color online) Determination of the “non-generic” arcs for the driving shapes  $f_2$  (a) and  $f_3$  (b). The color code in the lower panels depicts  $G(t, \tau_\epsilon)$ , while the horizontal dashed lines mark the generic solutions of Eq. (31) at multiples of  $T/2$ . The solid lines represent numerical solutions of Eq. (31). Significant contributions to  $W(\tau_\epsilon, \tau_A)$  are determined by the solutions of the transcendental equations (31) and (32), i.e. the cuts of  $G(t, \tau_\epsilon)$  along the solid and dashed lines. Projecting these solutions on the  $\tau_\epsilon$  axis (hinted by vertical dotted lines) results in the arc structures plotted in the upper panels and in Figs. 1(h) and 1(i).

which describe one-dimensional manifolds in the Fourier space  $(\tau_\epsilon, \tau_A)$ . They correspond to the arcs in Figs. 1(g)–(i). Practically, the arc structure is obtained in the following way. One determines from  $g(t_i, \tau_\epsilon) = 0$  all zeros  $t_i(\tau_\epsilon)$  and inserts them into Eq. (32) which yields relations of the type  $\tau_A^{(i)}(\tau_\epsilon)$ .

Obviously,  $\tau_A = \tau_\epsilon = t = 0$  is a trivial solution for any driving shape  $f(t)$ . Thus, the Fourier transformed of all LZSM patterns exhibits a peak at the origin and, owing to the periodicity of the driving, at multiples of  $T$ .

Two generic arcs can be found analytically if the driving obeys time-reversal symmetry,  $f(t - t_s) = f(-t - t_s)$  (without loss of generality, we henceforth assume  $t_s = 0$ ). Then Eq. (31) possesses the solutions  $t_1 = 0$  and, owing to the  $T$ -periodicity of  $f$ ,  $t_2 = T/2$ . They provide the arcs

$$\tau_A^{(1)} = 2F(\tau_\epsilon/2), \quad (33)$$

$$\tau_A^{(2)} = 2F(\tau_\epsilon/2 + T/2), \quad (34)$$

which are in agreement with Ref. [14].

If a symmetric driving  $f$  has only one minimum and one maximum per period, such as  $f_1$  or  $f(t) = \cos(\Omega t)$ ,  $t_1$  and  $t_2$  are the only roots of Eq. (31). Then the arc structure for symmetric driving can be obtained fully analytically. This fact is of practical use if one employs LZSM interference to determine decoherence properties of a qubit via the arc decay [13].

In all other cases, i.e., when  $f$  is not symmetric or if it possesses more than two extrema per period, we have to

solve Eq. (31) numerically to obtain also “non-generic” arcs. For the symmetric driving  $f_2$ , this leads to the ellipse-shaped solutions sketched in the lower panel of Fig. 5(a). Upon reducing the harmonic with frequency  $2\Omega$ , they shrink and eventually vanish. Together with the generic solution, we obtain the structure shown in the upper panel of Fig. 5(a). In particular, there is a region in which the arc splits into two branches. This prediction is quantitatively confirmed by the numerical solution of the full problem shown in Fig. 1(h).

If  $f$  is not time-reversal symmetric, we generally have to determine all  $t_i$  numerically. For the driving shape  $f_3$ , this procedure is visualized in Fig. 5(b), where the solid lines in the lower panel depict the zeros of  $g(t, \tau_\epsilon)$  which define two independent manifolds  $t_i(\tau_\epsilon)$  and those related by the time shift  $t \rightarrow t + T$ . The corresponding arc structure shown in the upper panel agrees with the one obtained numerically which is shown in Fig. 1(i).

### B. Weak dissipation

In the limit of weak dissipation,  $\Gamma \ll \Delta_n$ , the resonance width in Eq. (23) becomes  $\Gamma_n^* = |\Delta_n|/\sqrt{2}$ , so that we have to evaluate the Fourier transform of  $\sum_n |\Delta_n(A)|$ . This represents a rather difficult task and, thus, we only discuss its implications on a qualitative level.

A main effect of the cusps stemming from the absolute value is the emergence of higher harmonics, cf. the Fourier transform of expressions such as  $|\cos(\Omega t)|$ . Accordingly, in the Fourier transform of our interference patterns, we find arcs of higher order as can be appreciated in Figs. 1(g)–(i). To be specific, the arcs given by Eqs. (33) and (34) are generalized to

$$\tau_A = 2kF(\tau_\epsilon/2k + k'T/2k), \quad (35)$$

where  $k = 1, 2, 3, \dots$  and  $k' = 0, 1, \dots, 2k - 1$ . This prediction agrees with our numerical findings shown in Figs. 1(g) and 1(h). From a theoretical point of view, it is interesting to see that arcs of higher order are found already within a two-level description, i.e., within the most basic model for LZSM interference. Thus, their emergence does not require the consideration of further levels or non-linearities.

## V. DECAY OF THE ARC STRUCTURE

A promising application of LZSM interferometry is to determine microscopic model parameters such as the dimensionless dissipation strength  $\alpha$ . In Ref. [13], this was performed by comparing the decay of the arc structure of measured LZSM patterns with corresponding theoretical data. This application raises interest in the corresponding decay rates as a function of the bath parameters which are the dissipation strength and the temperature. Some examples for the arc decay are shown in

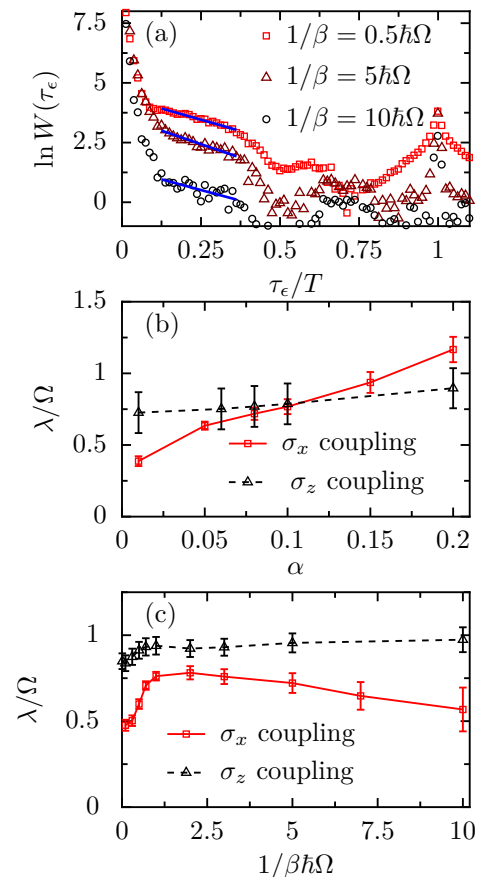


FIG. 6. (Color online) Analysis of the principal arc for the driving  $f(t) = \cos(\Omega t)$  and system-bath coupling with  $\Delta = 0.5\Omega$ . (a) Fourier transform of the interference pattern,  $W(\tau_\epsilon, \tau_A)$  along the principal arc  $\tau_A = 2F(\tau_\epsilon/2)$  for  $\sigma_x$  coupling and  $\alpha = 0.05$ . The symbols show numerical results for different temperatures  $1/\beta$ , while the straight lines are fits to an exponential decay. (b) Decay rate  $\lambda$  for temperature  $1/\beta = 0.5\hbar\Omega$  as a function of the dissipation strength  $\alpha$ . The error bars are determined by slightly varying the fit range. (c) Decay rate as a function of the temperature for dissipation strengths  $\alpha = 0.05$ .

Fig. 6(a). It can be appreciated that in the vicinity of  $\tau_\epsilon \approx T/4$ , the Fourier amplitude decays exponentially,  $W(\tau_\epsilon) \propto \exp(-\lambda\tau_\epsilon)$ , where  $\lambda$  can be determined by a numerical fit procedure. Figures 6(b) and 6(c) show the result as a function of the dissipation strength and the temperature, respectively.

For longitudinal bath coupling, the rate exhibits a rather weak parameter dependence. A possible reason for this is that dissipative decays happen mainly during the short stages when the levels cross. Therefore the effective decoherence rate is always much smaller than the “natural” width of the asymmetric peaks given by  $\Delta_n$ , cf. Fig. 4(a) and Eq. (21). At first sight, this weak parameter dependence seems not in accordance with the LZSM patterns for open quantum dots with a bath coupling via  $\sigma_z$  [13]. Notice however that the open double quantum



dot used there is beyond the present model. First, the description of electron transport requires one to take more states and different electron numbers into account, especially when also spin effects play a role. Second, there the dot-lead coupling is responsible for the main dissipative effects, while the bath coupling represents a perturbation and does not influence the qualitative behavior.

For the transverse bath coupling via  $\sigma_x$ , by contrast,  $\lambda$  grows significantly and monotonically with the dissipation strength  $\alpha$ , a feature that is essential for the fixing of  $\alpha$  from measured data. The behavior as a function of the temperature is more involved and even non-monotonic. For very low temperatures, the decay rate starts with a value  $\lambda \approx 0.4\Omega$ , followed by a steep increase until the thermal energy matches the photon energy,  $k_B T \approx \hbar\Omega$ . Then a slow decay sets in which lasts until eventually the range of exponential decay becomes so small that the fitting procedure is no longer reasonable.

## VI. CONCLUSIONS

We have developed a comprehensive picture of LZSM interference for the spin-boson model and thereby extended previous results to arbitrary shapes of the periodic driving and a generalized qubit-bath coupling. Our central quantity of interest was the time-averaged population of the excited state of the undriven qubit. For its numerical computation, we have employed a Bloch-Redfield master equation decomposed into the Floquet states of the driven qubit, while avoiding any rotating-wave approximation even in its moderate form. Thus, our long-time solution contains the full information about the coherences.

The interference patterns in “real space”, i.e., as a function of the detuning and the driving amplitude turned out to be governed by the qubit operator that couples to the environmental degrees of freedom. By contrast, the shape of the driving is of minor relevance. In particular, we found that for a bath coupling that is transverse with respect to the driving, the resonances are Lorentzians, while they possess an anti-symmetric structure in the longitudinal case. By a mapping to an effective static Hamiltonian we have obtained Bloch equations which yield expression for the LZSM patterns in agreement with numerical results. As a further feature, the LZSM pattern exhibits a triangular background which can be explained within an adiabatic approximation for the full time-dependent Bloch equations. Moreover, in the presence of both a transverse and a longitudinal bath coupling, the influence of the transverse coupling prevails.

The Fourier transform of the LZSM patterns provide a complementary picture. While the bath coupling is of minor influence, the observed arc structure reflects the shape of the driving, as can be predicted from the solution of our effective Bloch equations. For a driving with time-reversal symmetry, the arcs are given by the inte-

gral of the driving. In addition, they may develop side branches which can be explained within our analytical approach, but their determination requires the moderate effort of numerically solving a transcendental equation. The same numerical procedure also serves for the case of asymmetric driving.

A promising application of LZSM interferometry is the fixing of dissipative parameters by comparing the arc decay for experimental and theoretical data. In this spirit, we have performed the corresponding theoretical calculations. They show that for transverse bath coupling, the decay rate increases significantly with dissipation strength and temperature, as long as the thermal energy does not exceed the energy quantum of the driving. Thus, in particular for predominantly transverse coupling and low temperatures, LZSM interference represents a useful tool for analyzing decoherence properties. For purely longitudinal bath coupling, by contrast, the arcs decay depends only weakly on dissipation.

Our investigation reveals that already the LZSM pattern of a qubit is quite intriguing. It may become even more involved for Landau-Zener scenarios with three or more levels [27, 28] which are relevant when spin effects enter [29] or for a qubit that couples to additional degrees of freedom such as, e.g., an exciton in a photonic crystal with a coupling modulated by a surface-acoustic [30]. LZSM interferometry for such setups represents an emerging field of investigation.

## ACKNOWLEDGMENTS

We like to thank Florian Forster and Stefan Ludwig for helpful discussions. This work was supported by the Deutsche Forschungsgemeinschaft via Sonderforschungsbereich SFB 631 (Project A5) and by the Spanish Ministry of Economy and Competitiveness through grant no. MAT2011-24331.

## Appendix A: Bloch equations

In order to derive an equation of motion for the *time-independent* qubit, we start from the master equation (4). and notice that for the Ohmic spectral density  $J(\omega) = 2\pi\alpha\omega$ , the anti-symmetric bath correlation function (6) becomes  $A(\tau) = 2\pi\alpha\delta'(\tau)$ . This has for the  $\tau$ -integral in Eq. (4) the consequence that the Heisenberg operator  $\tilde{X}$  turns into its time-derivative evaluated at  $\tau = 0$ . Thus it can be expressed by the commutator  $i[H, X]$  and we obtain

$$\dot{\rho} = -i[H, \rho] - \frac{1}{4}[X, Q, \rho] + \frac{\pi\alpha}{4}[X, \{[H, X], \rho\}], \quad (\text{A1})$$

where the second term depends on the coherent qubit dynamics via the operator

$$Q = \frac{1}{2} \int_{-\infty}^{+\infty} d\tau S(\tau) \tilde{X}(-\tau). \quad (\text{A2})$$

Since all analytical results of the main paper can be mapped by a permutation of the Pauli matrices to a qubit in its eigenbasis with a qubit-bath coupling via either  $X = \sigma_x$  or  $X = \sigma_z$ , we consider the Hamiltonian

$$H = \frac{E}{2}\sigma_z. \quad (\text{A3})$$

For  $X = \sigma_x$ , the Heisenberg operator in Eq. (A2) reads  $\tilde{\sigma}_x(-\tau) = \sigma_x \cos(E\tau) - \sigma_y \sin(E\tau)$ . With this expressions at hand, it is straightforward to evaluate the operator  $Q$  and to map the master equation (A1) to an equation of motion for the Bloch vector  $\vec{s} = \text{tr}(\vec{\sigma}\rho)$ . After some algebra and a rotating-wave approximation, we find the Bloch equation

$$\frac{d}{dt}\vec{s} = \begin{pmatrix} -\Gamma/2 & E & 0 \\ -E & -\Gamma/2 & 0 \\ 0 & 0 & -\Gamma \end{pmatrix} \vec{s} + \begin{pmatrix} 0 \\ 0 \\ \pi\alpha E \end{pmatrix}, \quad (\text{A4})$$

where the rate

$$\Gamma = \pi\alpha E \coth(\beta E/2) \quad (\text{A5})$$

depends on the qubit splitting and at low temperatures,  $kT \ll E$ , it becomes  $\Gamma = \pi\alpha|E|$ .

For  $\sigma_z$  coupling, the Heisenberg operator of the bath coupling is time independent,  $\tilde{\sigma}_z(-\tau) = \sigma_z$ , so that the  $\tau$ -integral yields the Fourier transform of the symmetric spectral density at zero frequency. Moreover, the last term of the master equation (A1) vanishes. Accordingly, the Bloch equation is homogeneous and reads

$$\frac{d}{dt}\vec{s} = \begin{pmatrix} -\Gamma_\varphi & E & 0 \\ -E & -\Gamma_\varphi & 0 \\ 0 & 0 & 0 \end{pmatrix} \vec{s}, \quad (\text{A6})$$

where the dephasing rate

$$\Gamma_\varphi = 4\pi\alpha kT \quad (\text{A7})$$

vanishes in the zero-temperature limit. Notice that the  $z$ -component of the Bloch vector is conserved.

- 
- [1] L. D. Landau, Phys. Z. Sowjetunion **2**, 46 (1932).  
[2] C. Zener, Proc. R. Soc. London, Ser. A **137**, 696 (1932).  
[3] E. C. G. Stueckelberg, Helv. Phys. Acta **5**, 369 (1932).  
[4] E. Majorana, Nuovo Cimento **9**, 43 (1932).  
[5] S. N. Shevchenko, S. Ashhab, and F. Nori, Phys. Rep. **492**, 1 (2010).  
[6] W. D. Oliver, Y. Yu, J. C. Lee, K. K. Berggren, L. S. Levitov, and T. P. Orlando, Science **310**, 1653 (2005).  
[7] M. Sillanpää, T. Lehtinen, A. Paila, Y. Makhlin, and P. Hakonen, Phys. Rev. Lett. **96**, 187002 (2006).  
[8] C. M. Wilson, T. Duty, F. Persson, M. Sandberg, G. Johansson, and P. Delsing, Phys. Rev. Lett. **98**, 257003 (2007).  
[9] D. M. Berns, M. S. Rudner, S. O. Valenzuela, K. K. Berggren, W. D. Oliver, L. S. Levitov, and T. P. Orlando, Nature (London) **455**, 51 (2008).  
[10] J. Stehlik, Y. Dovzhenko, J. R. Petta, J. R. Johansson, F. Nori, H. Lu, and A. C. Gossard, Phys. Rev. B **86**, 121303(R) (2012).  
[11] E. Dupont-Ferrier, B. Roche, B. Voisin, X. Jehl, R. Wacquez, M. Vinet, M. Sanquer, and S. De Franceschi, Phys. Rev. Lett. **110**, 136802 (2013).  
[12] J. Li, M. P. Silveri, K. S. Kumar, J.-M. Pirkkalainen, A. Vepsäläinen, W. C. Chien, J. Tuorila, M. A. Sillanpää, P. J. Hakonen, E. V. Thuneberg, and G. S. Paraoanu, Nature Comm. **4**, 1420 (2013).  
[13] F. Forster, G. Petersen, S. Manus, P. Hänggi, D. Schuh, W. Wegscheider, S. Kohler, and S. Ludwig, Phys. Rev. Lett. **112**, 116803 (2014).  
[14] M. S. Rudner, A. V. Shytov, L. S. Levitov, D. M. Berns, W. D. Oliver, S. O. Valenzuela, and T. P. Orlando, Phys. Rev. Lett. **101**, 190502 (2008).  
[15] M. Grifoni and P. Hänggi, Phys. Rep. **304**, 229 (1998).  
[16] S. Kohler, T. Dittrich, and P. Hänggi, Phys. Rev. E **55**, 300 (1997).  
[17] R. Blümel, A. Buchleitner, R. Graham, L. Sirko, U. Smilansky, and H. Walter, Phys. Rev. A **44**, 4521 (1991).  
[18] J. Lehmann, S. Kohler, P. Hänggi, and A. Nitzan, Phys. Rev. Lett. **88**, 228305 (2002).  
[19] F. Großmann and P. Hänggi, Europhys. Lett. **18**, 571 (1992).  
[20] Y. Kayanuma, Phys. Rev. A **50**, 843 (1994).  
[21] A. M. Satanin, M. V. Denisenko, A. I. Gelman, and F. Nori, arXiv:1305.4800 [cond-mat].  
[22] M. Strass, P. Hänggi, and S. Kohler, Phys. Rev. Lett. **95**, 130601 (2005).  
[23] A. Izmalkov, S. H. W. van der Ploeg, S. N. Shevchenko, M. Grajcar, E. Il'ichev, U. Hübner, A. N. Omelyanchouk, and H.-G. Meyer, Phys. Rev. Lett. **101**, 017003 (2008).  
[24] J. Thingna, J.-S. Wang, and P. Hänggi, J. Chem. Phys. **136**, 194110 (2012).  
[25] K. M. Fonseca-Romero, S. Kohler, and P. Hänggi, Chem. Phys. **296**, 307 (2004).  
[26] T. M. Stace, A. C. Doherty, and S. D. Barrett, Phys. Rev. Lett. **95**, 106801 (2005).  
[27] M. N. Kiselev, K. Kikoin, and M. B. Kenmoe, EPL **104**, 57004 (2013).  
[28] A. M. Satanin, M. V. Denisenko, S. Ashhab, and F. Nori, Phys. Rev. B **85**, 184524 (2012).  
[29] H. Ribeiro, G. Burkard, J. R. Petta, H. Lu, and A. C. Gossard, Phys. Rev. Lett. **110**, 086804 (2013).  
[30] R. Blattmann, H. J. Krenner, S. Kohler, and P. Hänggi, Phys. Rev. A **89**, 012327 (2014).